

Magnetospheric cavity modes driven by solar wind dynamic pressure fluctuations

S. G. Claudepierre,¹ M. Wiltberger,² S. R. Elkington,³ W. Lotko,⁴
and M. K. Hudson¹

Received 8 May 2009; accepted 2 June 2009; published 1 July 2009.

[1] We present results from Lyon-Fedder-Mobarry (LFM) global, three-dimensional magnetohydrodynamic (MHD) simulations of the solar wind-magnetosphere interaction. We use these simulations to investigate the role that solar wind dynamic pressure fluctuations play in the generation of magnetospheric ultra-low frequency (ULF) pulsations. The simulations presented in this study are driven with idealized solar wind input conditions. In four of the simulations, we introduce monochromatic ULF fluctuations in the upstream solar wind dynamic pressure. In the fifth simulation, we introduce a continuum of ULF frequencies in the upstream solar wind dynamic pressure fluctuations. In this numerical experiment, the idealized nature of the solar wind driving conditions allows us to study the magnetospheric response to only a fluctuating upstream dynamic pressure, while holding all other solar wind driving parameters constant. The simulation results suggest that ULF fluctuations in the solar wind dynamic pressure can drive magnetospheric ULF pulsations in the electric and magnetic fields on the dayside. Moreover, the simulation results suggest that when the driving frequency of the solar wind dynamic pressure fluctuations matches one of the natural frequencies of the magnetosphere, magnetospheric cavity modes can be energized.
Citation: Claudepierre, S. G., M. Wiltberger, S. R. Elkington, W. Lotko, and M. K. Hudson (2009), Magnetospheric cavity modes driven by solar wind dynamic pressure fluctuations, *Geophys. Res. Lett.*, *36*, L13101, doi:10.1029/2009GL039045.

1. Introduction

[2] Several observational studies suggest that some dayside magnetospheric ultra-low frequency (ULF) pulsations may be directly driven by ULF fluctuations in the solar wind dynamic pressure. For example, *Kepko and Spence* [2003] examine six events where discrete ULF fluctuations are observed in the solar wind dynamic pressure. The authors show a one-to-one correspondence between these solar wind dynamic pressure fluctuations and discrete spectral peaks in dayside GOES magnetic field data. The authors argue that the dayside magnetospheric ULF pulsa-

tions are directly driven by the corresponding solar wind dynamic pressure fluctuations. Other observational studies [*Sibeck et al.*, 1989; *Korotova and Sibeck*, 1995; *Matsuoka et al.*, 1995; *Han et al.*, 2007] also suggest that solar wind dynamic pressure fluctuations can directly drive dayside magnetic field ULF pulsations. Very recent work [*Viall et al.*, 2009] concludes that approximately half of the variations observed in magnetospheric ULF waves are likely directly driven by solar wind dynamic pressure fluctuations. In this study we investigate, through the use of global magnetohydrodynamic (MHD) simulations, the magnetospheric response to ULF solar wind dynamic pressure (henceforth, p_{dyn}) fluctuations. Here, ‘ULF’ refers to frequencies in the 0.5 to 50 mHz range (Pc3-Pc5 bands [*Jacobs et al.*, 1964]), though we make no distinction between continuous and irregular magnetospheric pulsations.

2. Methodology

[3] The details of the Lyon-Fedder-Mobarry (LFM) simulation code, the computational grid, and the numerical techniques used to solve the single-fluid ideal MHD equations are given by *Lyon et al.* [2004]. The solar wind input conditions form the outer boundary condition in the LFM simulation. For the inner boundary condition, the magnetospheric portion of the code couples to an empirical ionospheric model, which forms a two-way coupling between the simulation ionosphere and magnetosphere [*Wiltberger et al.*, 2009]. The LFM simulation does not contain a plasmaspheric model and, thus, number densities in the simulation inner magnetosphere are lower than what is typically observed in the real magnetosphere. Also, as discussed by *Lyon et al.* [2004], the LFM utilizes the Boris correction when solving the ideal MHD equations, where the speed of light is replaced by a smaller value to increase the allowable time step. The simulation code remains stable, however, when wave propagation speeds exceed the assumed speed of light, roughly 1,100 km/s in the LFM inner magnetosphere. We present results from five LFM simulations: four driven by monochromatic upstream p_{dyn} fluctuations and one driven by a continuum of frequencies in the upstream p_{dyn} fluctuations.

[4] Solar wind dynamic pressure is not an explicit input in the LFM simulation and we choose to introduce the dynamic pressure fluctuations via the upstream number density component, as opposed to the velocity component. Solar wind observations typically show that p_{dyn} variations are carried by the solar wind number density, and not the velocity [e.g., *Kepko and Spence*, 2003; *Han et al.*, 2007]. For the four monochromatic simulations, we impose a number density time series, $n(t)$, at the LFM upstream

¹Department of Physics and Astronomy, Dartmouth College, Hanover, New Hampshire, USA.

²High Altitude Observatory, National Center for Atmospheric Research, Boulder, Colorado, USA.

³Laboratory for Atmospheric and Space Physics, University of Colorado, Boulder, Colorado, USA.

⁴Thayer School of Engineering, Dartmouth College, Hanover, New Hampshire, USA.

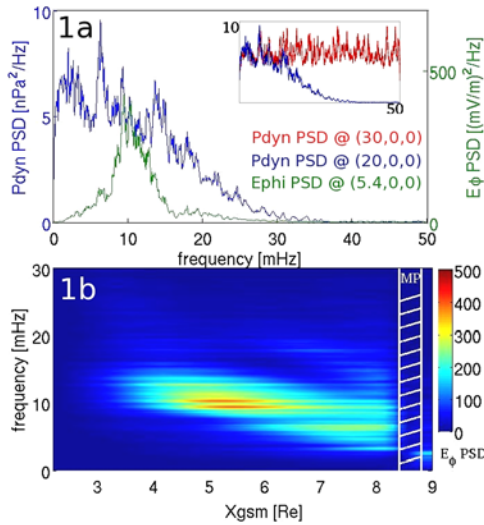


Figure 1. (a) Dynamic pressure PSD in the upstream solar wind (blue trace) and E_ϕ PSD at $5.4 R_E$ on the noon meridian (green trace), from the continuum simulation. Inset: p_{dyn} PSD input at the LFM upstream boundary (red trace) and p_{dyn} PSD in the upstream solar wind (blue trace). (b) E_ϕ PSD plotted along the entire noon meridian in the continuum simulation. The location of the magnetopause is indicated by the shaded region.

boundary at $x = 30 R_E$ of the form: $n(t) = n_0 + \delta n \sin(\omega t)$. The four monochromatic driving frequencies chosen for analysis in this study are 5, 10, 18, and 25 mHz and the background number density, n_0 , is 5 particles/cm³. In the 5 and 10 mHz simulations, $\delta n = 1$ (20% oscillation amplitude); in the 18 mHz simulation, $\delta n = 1.5$ (30% oscillation amplitude); and in the 25 mHz simulation, $\delta n = 2$ (40% oscillation amplitude). The larger oscillation amplitudes for the input time series in the 18 mHz and 25 mHz runs are used to combat the effects of a numerical attenuation/filtering of higher frequency components in the LFM simulation. For the fifth simulation, we impose a continuum of ULF frequencies in the input number density time series: $n(t) = n_0 + 0.05 \sum_j \sin(\omega_j t + \phi_j)$. Here, we create an input spectrum with fluctuations in the 0 to 50 mHz band with a 0.1 mHz spacing between frequency components (j ranges from 0 to 500) and we add a random phase, ϕ_j , to each frequency component. The value of 0.05 in the above equation is chosen so that the root-mean square (RMS) amplitude of the continuum input number density time series is roughly equal to that of the monochromatic input number density time series (with 20% oscillation amplitudes). In addition, in all five simulations, we introduce an appropriate out of phase oscillation in the input sound speed time series, so as to hold the thermal pressure constant in the upstream solar wind ($p_{th} \propto nC_s^2$). The background sound speed upon which the out of phase oscillation is imposed is 40 km/s. The remaining idealized solar wind input parameters are the same in all five simulations and held constant for the entire duration (4 hours) of the simulations: $\mathbf{B} = (0, 0, -5)$ nT and $\mathbf{v} = (-600, 0, 0)$ km/s.

[5] The power spectral density (PSD) of the continuum simulation input p_{dyn} time series is shown as the red trace in the inset of Figure 1a. Note the relatively uniform distribu-

tion of wave power over the 0 to 50 mHz frequency band. The blue trace in the inset panel shows the PSD of the p_{dyn} time series taken at $(20, 0, 0) R_E$ in the solar wind (GSM coordinates are used throughout) in the continuum simulation. Comparing the red and blue traces, we see that the spectral profile imposed at the upstream boundary (red trace) has been significantly altered by the time the fluctuations reach $(20, 0, 0) R_E$ (blue trace). This filtering/attenuation of the higher frequency spectral components, to be discussed in a follow-up paper, is an expected artifact of the numerics in the LFM (J. Lyon, personal communication, 2008). Nonetheless, there is significant ULF wave power in the 0 to 20 mHz frequency band in the upstream p_{dyn} driving, which is the spectral profile that drives the magnetosphere.

[6] The filtering/attenuation of the input time series in the continuum simulation results in upstream driving at $(20, 0, 0) R_E$ on the order of 13%, reduced from the roughly 20% value imposed at the upstream boundary (in the RMS sense described above). As the inset of Figure 1a suggests, the filtering/attenuation reduces the amplitude of the upstream p_{dyn} driving at $(20, 0, 0) R_E$ to 24% in the 18 mHz simulation (input = 30%) and 15% in the 25 mHz simulation (input = 40%). Finally, we note that upstream p_{dyn} driving in the 13–24% range is reasonable when compared with the observational work discussed above and is at the lower end of what has been reported.

3. Simulation Results

[7] In all five simulations, the upstream p_{dyn} fluctuations launch earthward propagating compressional MHD waves near the subsolar bow shock. These waves propagate through the magnetosheath and then enter the magnetosphere near the subsolar magnetopause and propagate earthward through the dayside (not shown here). We examine the magnetospheric response in the equatorial plane in terms of the compressional magnetic and electric field components, B_z and E_ϕ . Along the noon meridian, the magnetospheric response in terms of B_z and E_ϕ fluctuation amplitude is roughly an order of magnitude greater than in the other field components.

[8] The green trace in Figure 1a shows the magnetospheric response to the upstream p_{dyn} fluctuations in the continuum simulation. Here, we plot power spectral density of the E_ϕ time series taken at $(5.4, 0, 0) R_E$ on the noon meridian. Note the clear preferential frequency in the magnetospheric response centered near 10 mHz. Comparing the fine structure in the spectral profile of the p_{dyn} fluctuations and the magnetospheric response near 10 mHz shows a one-to-one correspondence between the two traces. This suggests that the fluctuations in the magnetospheric E_ϕ are driven by the p_{dyn} fluctuations. Moreover, the fact that the magnetospheric response is strongly peaked near 10 mHz suggests that the magnetosphere is responding resonantly to the upstream p_{dyn} fluctuations, which contain a continuum of ULF frequencies. Although the magnetospheric response falls off sharply away from 10 mHz, one could perhaps argue that the response near 10 mHz is due to local peaks in the upstream driving spectrum near 10 mHz. The local peaks and valleys in the upstream driving spectrum are the result of the random phasing in the input time series and the discretization of the signal. We have conducted analogous

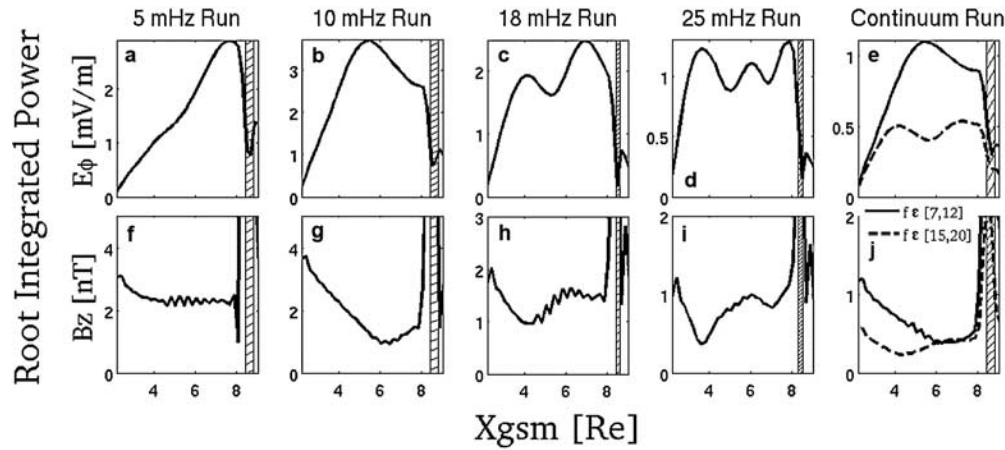


Figure 2. (a–e) E_ϕ and (f–j) B_z radial mode structure along the noon meridian for the five simulations. Root-integrated power is integrated over the driving band in the monochromatic simulations (Figures 2a–2d and 2f–2i) and over [7,12] and [15,20] mHz in the continuum simulation (Figures 2e and 2j). The location of the magnetopause is indicated by the shaded region.

simulations to the continuum simulation presented here, with only the random phasing changed, which moves the location of the local peaks and valleys in the upstream p_{dyn} driving spectrum. These simulations also show a magnetospheric response that is strongly peaked near 10 mHz. Thus, the magnetospheric response does not depend on the location of the local peaks and valleys in the upstream driving spectrum.

[9] To obtain a more global picture of the magnetospheric response, in Figure 1b we plot the E_ϕ PSD along the entire noon meridian in the continuum simulation. Here, distance along the noon meridian is plotted on the horizontal axis from $2.2 R_E$ (the inner boundary of the LFM simulation) to $9 R_E$. The subsolar magnetopause is located near $8.6 R_E$ on the noon meridian, though the magnetopause moves roughly $\pm 0.25 R_E$ about this location, due to the upstream p_{dyn} oscillations. This radial motion of the magnetopause is indicated by the shaded region in Figure 1b. Note that the green trace in Figure 1a can be extracted from Figure 1b by taking a vertical cut at $5.4 R_E$. The spectral profile along the entire noon meridian again shows a clear preferential frequency near 10 mHz for the magnetospheric response. Note that the frequency of the magnetospheric response does not change significantly with radial distance. However, the amplitude of the response near 10 mHz does depend on radial distance, with the maximum in wave power occurring between 5 and $6 R_E$. Finally, we note that there is an enhancement in the E_ϕ PSD near 6 mHz, that peaks just earthward of the magnetopause, and decays rapidly in the earthward direction. This is due to a local peak in the solar wind p_{dyn} fluctuations near 6 mHz (Figure 1a, blue trace) and the fact that this local peak in the driving spectrum lies near a resonant frequency of the magnetosphere.

[10] The results from the continuum simulation also suggest a secondary preferential frequency to the magnetospheric response, centered near 18 mHz. However, the upstream driving in the continuum simulation near 18 mHz is weaker than the driving near 10 mHz, due to the filtering/attenuation described above. Thus, the amplitude of the secondary magnetospheric response is weaker than the primary response near 10 mHz, and is not entirely resolved in Figure 1b due to the color scale used. As we will see below,

the amplitude of the secondary response near 18 mHz has two local maxima along the noon meridian, near 4 and $7 R_E$, in contrast with one local maximum for the amplitude of the primary (10 mHz) response between 5 and $6 R_E$.

[11] In Figure 2, we plot radial profiles of E_ϕ (Figures 2a–2e) and B_z (Figures 2f–2j) root-integrated power along the noon meridian for the five simulations in this study. Root-integrated power (RIP), plotted on the vertical axis in each of the ten panels, is defined as: $RIP = (\int_{f_a}^{f_b} P(f) df)^{\frac{1}{2}}$, where $P(f)$ is the power spectral density of the time series under consideration and the integration is carried out over a given frequency band of interest, $[f_a, f_b]$. In the four monochromatic simulations (Figures 2a–2d and 2f–2i), the RIP is integrated over the driving band, which we define as the 1 mHz frequency band centered on the driving frequency. In the the continuum simulation (Figures 2e and 2j), two RIP traces are shown, as there is no driving band in the continuum simulation. The solid trace is integrated over the frequency band [7,12] mHz, to pick up the primary spectral peak near 10 mHz, while the dashed trace is integrated over the frequency band [15,20] mHz to pick up the secondary spectral peak near 18 mHz. In each of the ten panels, distance along the noon meridian is plotted on the horizontal axis and the location of the subsolar magnetopause is indicated by the shaded regions near $8.5 R_E$.

[12] The five B_z plots Figures (2f–2j) show a strong amplitude maximum in B_z oscillation amplitude near the magnetopause that extends beyond the vertical scales used in the plots (the traces extend to a value on the order of 25 nT). These strong oscillation amplitudes near the magnetopause are due to the radial motion of the magnetopause and the subsequent changing dayside magnetopause current. As a side note, effects due to the LFM grid are clearly visible in the five B_z plots in Figures 2f–2j. For example, in the 5 mHz simulation (Figure 2f) there is a ‘sawtooth’ like structure in the radial profile between 5 and $7 R_E$. We do not attribute any physical significance to these features.

4. Discussion

[13] The simulation results presented above suggest a resonant response of the magnetosphere to solar wind

dynamic pressure fluctuations, with a standing wave structure along the noon meridian. The dependence of the magnetospheric response on the driving frequency can be explained by interpreting the simulation results as signatures of magnetospheric cavity mode oscillations [e.g., *Kivelson and Southwood, 1985*].

[14] In the simplest interpretation, magnetospheric MHD cavity modes can be thought of as standing waves in the electric and magnetic fields between a cavity inner and outer boundary. We consider the magnetopause to be the cavity outer boundary and the LFM simulation inner boundary at $2.2 R_E$ to be the cavity inner boundary. For the moment, we consider perfect conductor boundary conditions at the simulation inner boundary and magnetopause ($E_y, \partial_x B_z \rightarrow 0$). These boundary conditions impose half-wavelength standing waves in the radial direction between the simulation inner boundary and the magnetopause. Returning to the noon meridian radial profiles in Figure 2, we see that the simulation results support this standing wave interpretation. We argue that the E_ϕ and B_z radial profiles in the 10 mHz run (Figures 2b and 2g) are the signatures of the $n = 1$ cavity mode. Near the simulation inner boundary and magnetopause, E_ϕ has oscillation amplitude nodes and B_z has oscillation amplitude antinodes. Moreover, between the boundaries, E_ϕ has one oscillation amplitude antinode and B_z has one oscillation amplitude node, near $6 R_E$, all consistent with an $n = 1$ standing wave along the noon meridian. Note that the continuum simulation results suggest that the fundamental frequency of the magnetospheric cavity is near 10 mHz. Thus, the upstream driving frequency in the 10 mHz monochromatic simulation is near the fundamental resonant frequency of the magnetospheric cavity and the $n = 1$ radial eigenmode is excited.

[15] In the 5 mHz simulation, we argue that a cavity mode is not excited, which is supported by the continuum simulation results. The radial profile of E_ϕ along the noon meridian in the 5 mHz simulation (Figure 2a) suggests an evanescent decay of wave power, with E_ϕ wave power peaking just earthward of the magnetopause and decaying rapidly in the earthward direction. Monochromatic simulations with 1 mHz and 3 mHz driving, analogous to those presented here, show similar radial profiles in E_ϕ and B_z oscillation amplitude along the noon meridian. Thus, we argue that this is the characteristic behavior of dayside compressional magnetospheric disturbances under fluctuating solar wind p_{dyn} driving when cavity modes are not excited, an evanescent decay of wave energy earthward of the magnetopause. Finally, we note that the excitation of $n = 1$ cavity mode in the 10 mHz simulation is also able to explain the stronger E_ϕ response amplitude under 10 mHz monochromatic driving when compared with 5 mHz monochromatic driving. The peak value of E_ϕ oscillation amplitude along the noon meridian is roughly 3.0 mV/m in the 5 mHz simulation, whereas it is roughly 3.7 mV/m in the 10 mHz simulation. The only difference in the upstream driving in the two simulations is the driving frequency. Thus, the magnetosphere responds resonantly to the p_{dyn} fluctuations in the 10 mHz run and passively in the 5 mHz run.

[16] We now consider the radial profiles of E_ϕ and B_z wave power in the 18 mHz and 25 mHz monochromatic simulations. We argue that in the 18 mHz simulation the

$n = 2$ cavity mode is excited. Again, at the simulation inner boundary and magnetopause, E_ϕ has oscillation amplitude nodes, whereas B_z has amplitude antinodes. Moreover, near 4 and 7 R_E , E_ϕ has two oscillation amplitude antinodes, whereas B_z has two nodes. As discussed above, the continuum simulation results suggest that the frequency for an $n = 2$ oscillation lies near 18 mHz, which is the driving frequency in the 18 mHz simulation. Similarly, in the 25 mHz simulation, we argue that the $n = 3$ cavity mode is excited. In the E_ϕ profile, we see three clear oscillation amplitude antinodes near 4, 6 and 8 R_E . Two of the three corresponding nodes in the B_z profile are resolved near 4 and 7 R_E . The $n = 3$ interpretation also requires a third B_z node (likely between 4 and 7 R_E) that is not resolved in the simulation. We note that the B_z profile suggests that the RIP value for the unresolved node should be less than 1 nT. This would correspond to a peak-to-peak oscillation amplitude of roughly 2 nT or less, which is small when compared with background values on the order of 100's of nT. The LFM grid resolution (roughly 0.25 R_E here) coupled with the small oscillation amplitude may make it difficult to resolve three distinct B_z nodes in an $\approx 3 R_E$ range. The E_ϕ profile is consistent with the $n = 3$ cavity mode interpretation. Finally, we note that the radial profiles from the continuum simulation, when integrated around 10 mHz (solid trace) and 18 mHz (dashed trace), look qualitatively similar to the profiles in the 10 mHz and 18 mHz monochromatic simulations, respectively. This suggests that the $n = 1$ and $n = 2$ radial eigenmodes are simultaneously excited in the continuum simulation.

[17] The results from the continuum simulation suggest that the fundamental frequency of the magnetospheric cavity configuration is near 10 mHz. To derive an alternate estimate, we consider the cavity frequency in a simple box geometry configuration [e.g., *Wright, 1994*]:

$$f_n = \frac{V_A}{2a} n \quad \text{for } n = 1, 2, 3, \dots \quad (1)$$

where V_A is the Alfvén speed in the box, a is the box length in the X direction, and n is the quantization number. Here, we envision the box coordinates, (X, Y, Z) as the radial, azimuthal and field aligned directions in the LFM. The above equation for f_n assumes perfect conductor boundary conditions in the X -direction ($E_y, \partial_x B_z \rightarrow 0$). To evaluate the fundamental frequency in the box configuration, we consider $n = 1$ and only compare with LFM results from the 10 mHz and continuum simulations, as these are the only two simulations where the fundamental radial eigenmode is excited. We evaluate the fundamental frequency, f_1 , in the box with $a = 6.4 R_E$, the distance from the simulation inner boundary to the magnetopause, along the noon meridian. A value for the constant Alfvén speed in the box, V_A , must also be chosen. By tracking the compressional wave fronts in the 10 mHz simulation, as they move earthward from the subsolar magnetopause along the noon meridian, we compute a phase speed, $V_{ph,x}$, of roughly 1,750 km/s. With this estimate for V_A , we obtain $f_1 \approx 22$ mHz. For quarter-wavelength modes in the X direction, the $2a$ in equation (1) is replaced by $4a$ and the fundamental cavity frequency is $f_1 \approx 11$ mHz, close to the result suggested by the continuum simulation. The fact that the quarter-wavelength

fundamental cavity frequency is closer to 10 mHz than the half-wavelength estimate and the fact that the electric field oscillation amplitude does not go entirely to zero at the magnetopause both suggest that quarter-wavelength modes may be a more appropriate boundary condition at the magnetopause.

[18] As discussed in section 2, the speed of light in the LFM is set to an artificially low value, which limits the Alfvén wave propagation speed. Above, we computed a phase speed of roughly 1,750 km/s for the p_{dyn} -driven waves in the 10 mHz simulation, which exceeds the speed of light in the simulation. Thus, the wave propagation characteristics of the p_{dyn} -driven waves are effected by the Boris correction. The Boris correction compensates for neglect of the displacement current in the ideal MHD equations, which reduces the phase speed when $V_A \sim c$.

[19] Finally, we emphasize that the results presented in this study do not necessarily imply that the fundamental cavity frequency of the real magnetosphere is near 10 mHz. A key factor controlling the fundamental frequency of the magnetospheric cavity is the Alfvén speed profile. The LFM simulations presented in this study do not have a plasmaspheric model and, thus, have number densities in the dayside equatorial plane that are much lower than in the real magnetosphere. For example, a typical value for the LFM number density near $(5,0,0) R_E$ is $0.1 \text{ particles/cm}^3$. A more realistic LFM number density profile in the equatorial plane, under development, would significantly lower the fundamental cavity frequency of the LFM magnetosphere (e.g., equation (1)). For this reason, we do not compare the LFM simulation results with the observations of magnetospheric ULF waves driven by p_{dyn} fluctuations discussed in section 1. The observational work [e.g., *Kepko and Spence, 2003*] typically looks at frequencies less than 5 mHz, while we have shown that the lowest cavity mode frequency that the LFM supports, for these upstream parameters, is approximately 10 mHz.

[20] **Acknowledgments.** The authors are grateful for thoughtful discussions with R. E. Denton and J. G. Lyon.

References

- Han, D.-S., H.-G. Yang, Z.-T. Chen, T. Araki, M. W. Dunlop, M. Nosé, T. Iyemori, Q. Li, Y.-F. Gao, and K. Yumoto (2007), Coupling of perturbations in the solar wind density to global Pi3 pulsations: A case study, *J. Geophys. Res.*, *112*, A05217, doi:10.1029/2006JA011675.
- Jacobs, J. A., Y. Kato, S. Matsushita, and V. A. Troitskaya (1964), Classification of geomagnetic micropulsations, *J. Geophys. Res.*, *69*, 180–181.
- Kepko, L., and H. E. Spence (2003), Observations of discrete, global magnetospheric oscillations directly driven by solar wind density variations, *J. Geophys. Res.*, *108*(A6), 1257, doi:10.1029/2002JA009676.
- Kivelson, M. G., and D. J. Southwood (1985), Resonant ULF waves: A new interpretation, *Geophys. Res. Lett.*, *12*, 49–52, doi:10.1029/GL012i001p00049.
- Korotova, G. I., and D. G. Sibeck (1995), A case study of transient event motion in the magnetosphere and in the ionosphere, *J. Geophys. Res.*, *100*, 35–46.
- Lyon, J. G., J. A. Fedder, and C. M. Mobarry (2004), The Lyon–Fedder–Mobarry (LFM) global MHD magnetospheric simulation code, *J. Atmos. Sol. Terr. Phys.*, *66*, 1333, doi:10.1016/j.jastp.2004.03.020.
- Matsuoka, H., K. Takahashi, K. Yumoto, B. J. Anderson, and D. G. Sibeck (1995), Observation and modeling of compressional Pi 3 magnetic pulsations, *J. Geophys. Res.*, *100*, 12,103–12,115.
- Sibeck, D. G., et al. (1989), The magnetospheric response to 8-minute period strong-amplitude upstream pressure variations, *J. Geophys. Res.*, *94*, 2505–2519, doi:10.1029/JA094iA03p02505.
- Viall, N. M., L. Kepko, and H. E. Spence (2009), Relative occurrence rates and connection of discrete frequency oscillations in the solar wind density and dayside magnetosphere, *J. Geophys. Res.*, *114*, A01201, doi:10.1029/2008JA013334.
- Wiltberger, M., R. S. Weigel, W. Lotko, and J. A. Fedder (2009), Modeling seasonal variations of auroral particle precipitation in a global-scale magnetosphere-ionosphere simulation, *J. Geophys. Res.*, *114*, A01204, doi:10.1029/2008JA013108.
- Wright, A. N. (1994), Dispersion and wave coupling in inhomogeneous MHD waveguides, *J. Geophys. Res.*, *99*, 159–167.
- S. G. Claudepierre and M. K. Hudson, Department of Physics and Astronomy, Dartmouth College, 6127 Wilder Lab, Room 105, Hanover, NH 03755, USA. (seth.g.claudepierre@dartmouth.edu)
- S. R. Elkington, Laboratory for Atmospheric and Space Physics, University of Colorado, 1234 Innovation Drive, Boulder, CO 80303, USA.
- W. Lotko, Thayer School of Engineering, Dartmouth College, 8000 Cummings Hall, Hanover, NH 03755, USA.
- M. Wiltberger, High Altitude Observatory, National Center for Atmospheric Research, 3450 Mitchell Lane, Boulder, CO 80301, USA.